Chinese Chemical Letters 36 (2025) 110045

Contents lists available at ScienceDirect

Chinese Chemical Letters

journal homepage: www.elsevier.com/locate/cclet

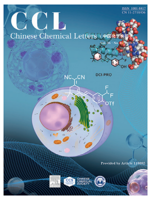

In situ synthesis of MnO_2 micro/nano-adjuvants for enhanced immunotherapy of breast tumors

Kun Chen[a,1], Huimin Lin[a,1], Xin Peng[d,1], Ziying Wu[e], Jingyue Dai[f], Yi Sun[d], Yaxuan Feng[a], Ziyi Huang[a], Zhiqiang Yu[c], Meng Yu[a,*], Guangyu Yao[b,*], Jigang Wang[a,g,h,i,*]

[a] *NMPA Key Laboratory for Research and Evaluation of Drug Metabolism & Guangdong Provincial Key Laboratory of New Drug Screening & Guangdong-Hong Kong-Macao Joint Laboratory for New Drug Screening, School of Pharmaceutical Sciences, Southern Medical University, Guangzhou 510515, China*
[b] *Breast Center, Nanfang Hospital, Southern Medical University, Guangzhou 510510, China*
[c] *Department of Laboratory Medicine, Dongguan Institute of Clinical Cancer Research, The Tenth Affiliated Hospital of Southern Medical University (Dongguan people's hospital), Dongguan 523018, China*
[d] *Department of Radiology, Nanjing Drum Tower Hospital, The Affiliated Hospital of Nanjing University Medical School, Nanjing 210008, China*
[e] *Department of General Surgery, Zhujiang Hospital, Southern Medical University, Guangzhou 510282, China*
[f] *Nurturing Center of Jiangsu Province for State Laboratory of AI Imaging & Interventional Radiology, Department of Radiology, Zhongda Hospital, School of Medicine, Southeast University, Nanjing 210009, China*
[g] *Department of Traditional Chinese Medicine and School of Pharmaceutical Sciences, Southern Medical University, Guangzhou 510515, China*
[h] *Department of Cardiology, Shenzhen Cardiovascular Minimally Invasive Medical Engineering Technology Research and Development Center, and Shenzhen Clinical Research Centre for Geriatrics, Shenzhen People's Hospital, The First Affiliated Hospital, Southern University of Science and Technology, Shenzhen 518020, China*
[i] *State Key Laboratory for Quality Ensurance and Sustainable Use of Dao-di Herbs, Artemisinin Research Center, and Institute of Chinese Materia Medica, China Academy of Chinese Medical Sciences, Beijing 100700, China*

ARTICLE INFO

Article history:
Received 27 March 2024
Revised 20 May 2024
Accepted 22 May 2024
Available online 23 May 2024

Keywords:
Cancer immunotherapy
Potassium permanganate
Manganese dioxide
Nanoadjuvants
In situ synthesis

ABSTRACT

This study presents an approach to enhanced cancer immunotherapy through the *in situ* synthesis of potassium permanganate ($KMnO_4$) derived manganese dioxide (MnO_2) micro/nano-adjuvants. Addressing the limitations of traditional immunotherapy due to patient variability and the complexity of the tumor microenvironment, our research establishes $KMnO_4$ as a potent immunomodulator that enhances the efficacy of anti-programmed death-ligand 1 (αPD-L1) antibodies. The *in situ* synthesized MnO_2 adjuvants in the tumor exhibit direct interactions with biological systems, leading to the reduction of MnO_2 to Mn^{2+} within the tumor, and thereby improving the microenvironment for immune cell activity. Our *in vitro* and *in vivo* models demonstrate $KMnO_4$'s capability to induce concentration-dependent cytotoxicity in tumor cells, triggering DNA damage and apoptosis. It also potentiates immunogenic cell death by upregulating calreticulin and high mobility group box 1 (HMGB1) on the cell surface. The combination of $KMnO_4$ with αPD-L1 antibodies substantially inhibits tumor growth, promotes dendritic cell maturation, and enhances $CD8^+$ T cell infiltration, resulting in a significant phenotypic shift in tumor-associated macrophages towards a pro-inflammatory M1 profile. Our findings advocate for further research into the long-term efficacy of $KMnO_4$ and its application in diverse tumor models, emphasizing its potential to redefine immune checkpoint blockade therapy and offering a new vista in the fight against cancer.

In the contemporary landscape of medical research and treatment, tumor immunotherapy has emerged as one of the most promising modalities against malignancies [1-3]. Distinct from conventional approaches like surgery, radiotherapy, and chemotherapy, immunotherapy aims to activate or enhance the patient's immune system, particularly its ability to recognize and eliminate tumor cells [4-6]. However, its efficacy is often constrained by individual patient variability and the complexity of the tumor microenvironment [7]. To address these challenges and broaden the applicability of immunotherapy, researchers are exploring strategies that combine immunoadjuvants with immunotherapeutic drugs [8-10]. Immunoadjuvants, serving as agents to bolster immune responses, synergize with therapeutic drugs to specifically enhance

---

[*] Corresponding authors.

E-mail addresses: yumeng999@smu.edu.cn (M. Yu), yaogy@smu.edu.cn (G. Yao), jgwang@icmm.ac.cn (J. Wang).

[1] These authors contributed equally to this work.

https://doi.org/10.1016/j.cclet.2024.110045

immune reactions at tumor sites, thereby improving treatment outcomes. Existing adjuvants such as inorganic nanoparticles [11-13], liposomes [14,15], and polymers [16-20] operate *via* various mechanisms to augment immune responses. Within this domain, manganese (Mn)-based adjuvants have attracted attention due to their unique advantages and great potential for clinical applications [21,22]. Mn, an essential trace element, plays a critical role in the function of numerous enzymes within biological systems. Mn-based adjuvants, by activating the stimulator of interferon genes pathway (STING) agonists through Mn^{2+}, not only significantly enhance the activity of STING agonists but also self-assemble into Mn-based nanomedicines, effectively delivering to immune cells and significantly amplifying anti-tumor immune responses while reducing the required dosage [23]. In particular, manganese chloride ($MnCl_2$), a key player in immunotherapy, has demonstrated substantial promise in phase I clinical trials with a controllable safety profile [24]. Acting as a pivotal activator of the cyclic GMP-AMP synthase (cGAS)-STING pathway, $MnCl_2$ is instrumental in amplifying the body's defense against tumor progression and metastasis by enhancing $CD8^+$ T cell infiltration and activity. Its synergistic use with immune checkpoint inhibitors marks a significant leap in cancer therapeutics, indicating a potential paradigm shift in the treatment of advanced metastatic solid tumors.

While Mn-based adjuvants hold considerable promise in enhancing immunotherapy outcomes, the complexity of their synthesis and the attendant high production costs present significant challenges [25-27]. Therefore, the development of a more readily accessible Mn-based adjuvant is of paramount importance. $MnCl_2$, despite its availability, is rapidly metabolized *in vivo*, leading to a reduced duration of therapeutic action. Thus, devising a Mn-based formulation that is both easy to obtain and exhibits prolonged activity compared to Mn^{2+} solutions remains a formidable challenge.

Potassium permanganate ($KMnO_4$), a well-known Mn-based oxidant, has drawn significant interest in the biomedical domain. By undergoing reactions with biomacromolecules such as bovine serum albumin (BSA), $KMnO_4$ has been instrumental in synthesizing MnO_2 adjuvants that exhibit the potential to enhance immune therapeutic efficacy [28-30]. Remarkably, clinical observations have suggested that $KMnO_4$ treatment leads to a considerable reduction in tumor symptoms, opening new pathways for its direct application in tumor immunotherapy enhancement [31]. Should $KMnO_4$ be developed as a Mn-based adjuvant, it would not only benefit from the ease of acquisition and simplicity of preparation but might also achieve a sustained release of Mn ions through *in situ* reactions with biomolecules and solid-state biological tissues to form micro and nano-sized MnO_2 particles. This could position $KMnO_4$ as a potent and promising agent in the arsenal of tumor immunotherapy. However, to date, direct applications of $KMnO_4$ as an immunotherapeutic enhancer in tumor treatments remain unreported and warrant further investigation.

In response, this work systematically explores the bioactivity of $KMnO_4$ in enhanced cancer immunotherapy and its potential mechanisms (Scheme 1). Our findings reveal that *in situ* injection of $KMnO_4$ into tumors effectively forms MnO_2 micro/nano-adjuvants, improving the hypoxic tumor microenvironment. This method, in conjunction with the anti-programmed death-ligand 1 (αPD-L1) antibodies, significantly enhances the efficacy of tumor immunotherapy. Firstly, the *in vitro* data reveals that $KMnO_4$ when interacting with tumor cells, biomacromolecules, and solid biological tissues, facilitates *in situ* generation of MnO_2 and its further conversion to Mn^{2+}. $KMnO_4$ also displays concentration-dependent cytotoxic effects on tumor cells, inducing DNA damage and apoptosis, and augments immunomodulation by increasing cell surface calreticulin (CRT) exposure and high mobility group box 1 (HMGB1) release, implying its role in inducing immunogenic cell death (ICD). Then, the *in vivo* studies show that the combined use of $KMnO_4$ with αPD-L1 antibodies significantly inhibits tumor growth, enhances dendritic cell (DC) maturation, increases $CD8^+$ T cell tumor infiltration, and induces a shift in tumor-associated macrophages (TAMs) toward the M1 phenotype, exhibiting pronounced anti-tumor effects. Additionally, the combination treatment strategy significantly extends the survival of tumor-bearing mice. Our work provides a new adjuvant option for tumor immunotherapy and lays the groundwork for future clinical applications of $KMnO_4$. While the use of $KMnO_4$ as an immunoadjuvant in tumor treatment is in its early stages of research, its unique mechanisms of action and therapeutic potential herald the possibility of more effective and safe treatment strategies for cancer patients in the future.

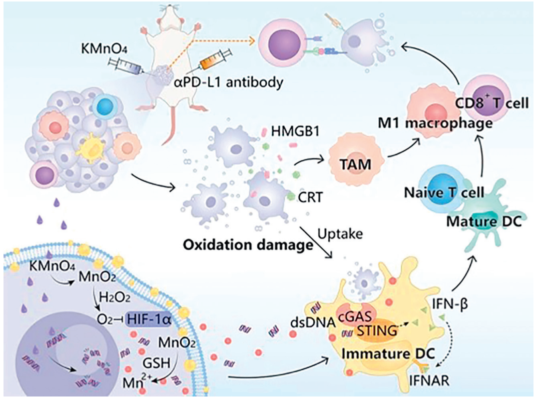

Scheme 1. Schematic illustration of the mechanism by which $KMnO_4$ enhances tumor ICB immunotherapy efficacy.

In an exploration of the interactions between $KMnO_4$ and various biological samples, including cells, biomolecules, and solid-state biological tissues, we systematically investigated the formation of manganese dioxide (MnO_2) precipitates. Optical microscopy images of 4T1 cells, before $KMnO_4$ treatment, presented a uniform size and spherical morphology in phosphate-buffered saline (PBS) solution post-enzymatic digestion, as shown in Fig. S1 (Supporting information). Enhanced optical microscopy images (Fig. 1a) revealed a homogeneous distribution of surface materials under the microscopic field, resembling the illustrated cell morphology depicted in Fig. 1a, without significant anisotropic distribution. Upon treatment with $KMnO_4$, a noticeable decrease in the transparency of tumor cells to light was observed, along with an increase in the contrast between the cells' grayscale and the background, as demonstrated in Fig. S2 (Supporting information). Despite maintaining their uniform size and spherical morphology, a significant quantity of granular particles exhibited an anisotropic distribution on the cellular membrane surface. High-magnification optical microscopy (Fig. 1b) clearly showed the cell membrane surfaces laden with dark brown particulate matter, distributed in an island-like pattern. For a detailed characterization of the changes in 4T1 cells post-$KMnO_4$ treatment and to identify the composition of the reaction products, high-resolution scanning electron microscopy (SEM), energy-dispersive X-ray (EDX) elemental imaging and spectroscopy, electron diffraction spectroscopy (EDS), and X-ray photoelectron spectroscopy (XPS) are utilized. SEM images (Figs. 1c and d) depicted a roughened cellular membrane surface post-treatment, covered with micro and nano-sized particles resembling a chocolate chip cookie as illustrated in Fig. 1c. This is attributed to the redox reaction between $KMnO_4$ and components like surface enzymes or unsaturated chemical bonds on the cell membrane, facilitating the rapid reduction of Mn^{7+} to Mn^{4+} and the subsequent deposition of MnO_2 particles. The formation of

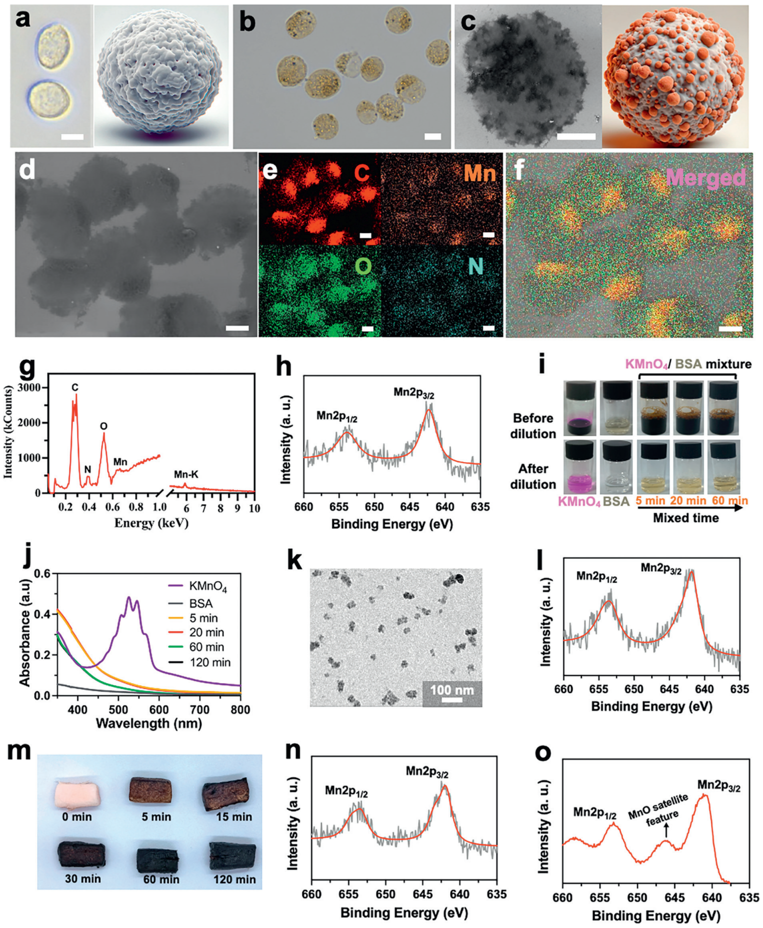

Fig. 1. The exploration of the interactions between $KMnO_4$ and various biological samples, including cells, biomolecules, and solid-state biological tissues. (a) Enlarged optical microscope photograph and 3D schematic of 4T1 cells. (b) Enlarged optical microscope photograph of 4T1 cells post-reaction with $KMnO_4$. (c) SEM image of 4T1 cells after reaction with $KMnO_4$. (d) SEM image of 4T1 cells following reaction with $KMnO_4$ and (e, f) their EDX spectroscopy elemental mapping images. Scale bar: 15 µm. (g) EDS of 4T1 cells after reaction with $KMnO_4$. (h) XPS spectrum of 4T1 cells after reaction with $KMnO_4$. (i) Images of solutions of $KMnO_4$, BSA, and $KMnO_4$ after different reaction times with BSA. (j) UV–vis absorption spectra images of $KMnO_4$, BSA, and the solutions of $KMnO_4$ with BSA after various reaction times. (k) TEM images of nanoparticles formed after the reaction of $KMnO_4$ with BSA. (l) XPS spectrum of nanoparticles formed after the reaction of $KMnO_4$ with BSA. (m) Photographic documentation of pork tissue's temporal reaction with $KMnO_4$ solution. (n) XPS spectra of pork tissue following the reaction with $KMnO_4$. (o) XPS spectra of the reaction products between $KMnO_4$ and 4T1 cells after treatment with GSH.

MnO_2 on the cell membrane post-$KMnO_4$ treatment was corroborated by EDX elemental quantitative analysis, EDS imaging, and XPS valence state analysis, as shown in Figs. 1e–h. EDX imaging revealed scattered Mn signals amidst predominant carbon (C), oxygen (O), and nitrogen (N) signals. EDS imaging (Fig. 1g), particularly the Mn characteristic X-ray Kα peak at 5.9 keV, further confirmed the deposition of Mn on the cell surface. XPS spectra (Fig. 1h) displayed two characteristic peaks at 652.4 and 641.5 eV, corresponding to the $2p_{3/2}$ and $2p_{1/2}$ spin-orbit coupling peaks of Mn^{4+} in MnO_2, which is similar to previously reported work [32], indicating a direct transformation of $KMnO_4$ to MnO_2 on the cell surface, vital for understanding the action mechanism of $KMnO_4$ at the cellular level.

Furthermore, $KMnO_4$ was shown to react with BSA, forming MnO_2-loaded nanoparticles. The reaction mixtures of $KMnO_4$ and BSA displayed intense brown and golden-yellow colors at high and low concentrations, respectively, as depicted in Fig. 1i. The UV–visible (UV–vis) absorption spectra (Fig. 1j) demonstrated a gradual blue shift in the absorption values of the mixture over a reaction time of 5–120 min, stabilizing around 120 min. Transmission electron microscopy (TEM) images (Fig. 1k) revealed uniformly sized nanoparticles (~20 nm), and XPS analysis (Fig. 1l) showed characteristic peaks at 652.4 and 641.5 eV, corresponding to the $2p_{3/2}$ and $2p_{1/2}$ spin-orbit coupling peaks of Mn^{4+} in MnO_2, confirming the successful loading of MnO_2 nanoparticles in the BSA-$KMnO_4$ reaction product.

Additionally, solid-state biological tissues, exemplified by porcine tissue treated with $KMnO_4$ *in vitro*, formed a dense brown coating after 120 min of reaction, as seen in Fig. 1m. The coating's area and color intensity progressively increased with reaction time. XPS analysis of the peeled-off, freeze-dried reaction product (Fig. 1n) revealed characteristic Mn^{4+} peaks at 652.4 and 641.5 eV, consistent with results from cellular and biomolecular analyses, indicating the formation and accumulation of MnO_2 within the solid tissue matrix. Upon treating tumor microenvironment mimics of high-reductive glutathione (GSH) solutions, with the $KMnO_4$-BSA reaction product, XPS analysis (Fig. 1o) revealed not only the characteristic peaks of MnO_2 at 652.4 and 641.5 eV but also an intermediate satellite peak indicative of MnO with Mn^{2+}, demonstrating the reductive transformation of MnO_2 to Mn^{2+} in the presence of GSH. Similar data related to the intermediate satellite peak indicative of MnO has also been reported in previously reported work [33]. These findings underscore the efficacy of $KMnO_4$ *in situ* formation of micro and nano-sized MnO_2 particles on tumor cells, biomolecules, and solid biological tissues through redox reactions with unsaturated bonds. Also, the generated MnO_2 particles are ca-

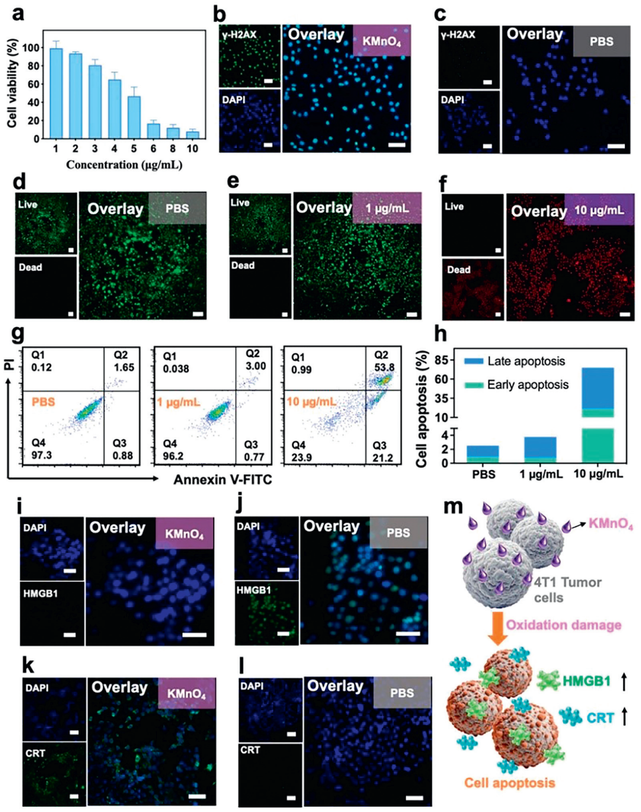

Fig. 2. (a) Analysis of cell viability after co-incubation of different concentrations of $KMnO_4$ solutions with 4T1 cells. Data are presented as mean ± standard deviation (SD) ($n = 5$). (b, c) The fluorescence image of 4T1 cells post-co-incubation with $KMnO_4$ solution, stained with γ-H2AX antibodies to visualize double-strand DNA breaks. (d–f) The calcein AM/propidium iodide staining method was used for live/dead cell staining of 4T1 cells after co-incubation of $KMnO_4$ solution with 4T1 cells. (g, h) Flow cytometry was utilized to assess apoptosis in 4T1 cells following co-incubation with $KMnO_4$ solutions of varying concentrations or PBS as the control. (i–l) The fluorescence imaging of 4T1 cells following incubation with $KMnO_4$ solution, labeled with HMGB1 and CRT antibodies, respectively. (m) Schematic diagram of $KMnO_4$-induced ICD in 4T1 cells. Scale bar: 100 μm.

pable of being further reduced to Mn^{2+} under GSH stimulus. The formation of MnO_2 and its reductive conversion in biologically relevant conditions highlight the versatility of $KMnO_4$ in generating functional micro/nano-structures for therapeutic purposes, establishing a foundational experimental basis for the advancement of Mn-based therapeutic modalities in the next cancer treatment.

To assess the oxidative damage efficacy of $KMnO_4$, 4T1 cells were co-incubated with varying concentrations of $KMnO_4$ for 24 h, and subsequent cell viability was assessed using the cell counting kit-8 (CCK8) assay. As depicted in Fig. 2a, $KMnO_4$ exhibited a highly concentration-dependent cytotoxic effect on 4T1 cells. At relatively low concentrations of $KMnO_4$ (2 μg/mL), 4T1 cells maintained over 85% viability. However, as the concentration of $KMnO_4$ increased, its toxicity to 4T1 cells significantly intensified. When co-incubated with a concentration of 10 μg/mL $KMnO_4$, cell viability dropped to less than 10%, indicating that the robust oxidative activity of $KMnO_4$ resulted in the demise of the majority of tumor cells. Additionally, the impact of $KMnO_4$ treatment on DNA double-strand break damage in tumor cells was assessed through the phosphorylated histone H2AX (γ-H2AX) antibody labeling. γ-H2AX is a phosphorylated form of the histone variant H2AX, which rapidly phosphorylates near the sites of DNA double-strand breaks as part of the DNA damage response, making it a sensitive marker for assessing DNA damage. The confocal microscopy images following immunofluorescence staining are depicted in the Figs. 2b and c, where the fluorescence signal of γ-H2AX is depicted in green, and the cell nuclei stained with 4′,6-diamidino-2-phenylindole (DAPI) are represented in blue. In the $KMnO_4$ treatment group, a significant enhancement in the green fluorescence signal of γ-H2AX was observed, indicating that $KMnO_4$ treatment induced a considerable amount of DNA double-strand breaks. Conversely, in the control group, the signal of γ-H2AX was relatively weaker, suggesting fewer occurrences of DNA double-strand breaks under PBS treatment conditions. The overlay of images illustrates the spatial correlation between the γ-H2AX signal and DAPI staining, providing an intuitive view of DNA damage distribution. These findings visually demonstrate the damaging effect of $KMnO_4$ on tumor cell DNA, laying the experimental foundation for further research on $KMnO_4$ as a potential anti-tumor agent.

Furthermore, we conducted live-dead cell staining on 4T1 cells using the calcein acetoxymethyl ester/propidium iodide (AM/PI) agent, and the experimental results are depicted in Figs. 2d–f. The cell viability of 4T1 cells is notably influenced by exposure to different concentrations of $KMnO_4$ solutions. Specifically, from Fig. 2d to Fig. 2f, the three sets of images represent the control group (PBS treatment), low concentration $KMnO_4$ treatment (1 μg/mL), and high concentration $KMnO_4$ treatment (10 μg/mL). In the control group, cells exhibit green fluorescence, indicating predominant cell viability. Upon treatment with low concentration $KMnO_4$, most cells maintain viability, as evidenced by the green fluorescence. However, with high concentration $KMnO_4$ treatment, there is a conspicuous rise in red fluorescence, suggesting a substantial rise in cell death rate. These findings align with the results of the cell viability assay depicted in Fig. 2a, further confirming the cytotoxic effect of $KMnO_4$-induced oxidative damage on cells, which is concentration-dependent.

Next, flow cytometry (FCM) combined with fluorescence labeling was employed to evaluate the specific apoptotic response of 4T1 breast cancer cells following co-incubation with $KMnO_4$. The results of flow cytometry in Figs. 2g and h illustrate the apoptosis detection of 4T1 cells treated with PBS (control group) and different concentrations of $KMnO_4$. In the flow cytometry plots, the horizontal axis represents Annexin V-fluorescein isothiocyanate (FITC) signal, while the vertical axis represents PI signal. The four quadrants depict cells in different states: Q1 (Annexin V-negative/PI-positive, dead cells), Q2 (Annexin V-positive/PI-positive, late apoptotic or dead cells), Q3 (Annexin V-positive/PI-negative, early apoptotic cells), and Q4 (Annexin V-negative/PI-negative, live cells). In the control group, most cells remained viable in quadrant Q4. However, with increasing $KMnO_4$ concentration from 1 μg/mL to 10 μg/mL, the proportion of early apoptotic cells (Q3) rose from 0.77% to 21.2%, and late apoptotic or dead cells (Q2) increased from 3.00% to 53.8%, indicating that the apoptosis rate of 4T1 cells is significantly boosted with the administration of high concentrations of $KMnO_4$.

Moreover, we evaluated the potential of $KMnO_4$ treatment to induce ICD in 4T1 cells by fluorescence imaging of CRT and HMGB1 extracellular release. During the process of ICD, CRT typically translocates from the endoplasmic reticulum to the outer surface of the cell membrane, serving as an "eat me" signal exposed on the cell surface. This translocation event constitutes an early phase of ICD, facilitating the recruitment and activation of DCs. Additionally, HMGB1, a non-histone nuclear protein, is conventionally associated with chromatin and involved in maintaining DNA structure. During ICD, HMGB1 is released from the cell nucleus to the extracellular milieu, representing a late-stage event. The extracellular release of HMGB1 serves as a signaling cue for immune system activation, as it can bind to receptors on the surface of DCs, such as Toll-like receptor 4 (TLR4), promoting their maturation and activation, thereby enhancing the immune response of T cells against tumors. Therefore, we initially performed fluorescence staining using anti-HMGB1 antibodies on the 4T1 cells. The fluorescence images (Figs. 2i and j) illustrate that in 4T1 cells subjected to $KMnO_4$ treatment, there is a notable reduction in the fluorescence signal of HMGB1, along with decreased co-localization with the cell nucleus. This suggests an augmented release of HMGB1 from the cell nucleus following $KMnO_4$ treatment. Additionally, fluorescence labeling of CRT was also performed on 4T1 cells after $KMnO_4$ treatment. The fluorescence images revealed a significant enhancement in CRT fluorescence signal in $KMnO_4$-treated cells compared to the PBS control group, particularly near the cell membrane (Figs. 2k and l). The results suggest that $KMnO_4$ promotes the exposure of CRT on the cell surface, which is another hallmark event of ICD. In conclusion, these observations suggest that the stimulation of 4T1 cells by $KMnO_4$ induces oxidation damage and immunogenic changes, potentially activating the immune system for the recognition and eradication of tumor cells *in vivo*, thereby enhancing tumor immunotherapy (Fig. 2m).

Therefore, we systematically investigated the synergistic effects of $KMnO_4$ combined with αPD-L1 antibody in tumor immunotherapy and elucidated the underlying mechanisms. All experiments involving mice were approved by the animal research center of Shenzhen People's Hospital, strictly following all applicable regulations. Four experimental groups were designed for *in vivo* treatment and exploration of immune mechanisms: (I) PBS (control group); (II) intraperitoneal injection of free αPD-L1 antibody; (III) intratumoral administration of $KMnO_4$; (IV) combined treatment with intraperitoneal injection of free αPD-L1 antibody and intratumoral administration of $KMnO_4$. The individual volume statistics of tumor growth under the four different treatment strategies are illustrated in Fig. S3 (Supporting information). The analysis of final tumor volume data indicated an average volume of 1261.91 mm^3 in the PBS group, 746.88 mm^3 in the αPD-L1 antibody group, 875.80 mm^3 in the $KMnO_4$ intratumoral administration group, and a significant reduction to 88.97 mm^3 in the combined intraperitoneal αPD-L1 antibody and intratumoral $KMnO_4$ treatment group. These findings demonstrate the remarkable efficacy of the combination therapy in inhibiting tumor growth, surpassing single-treatment modalities. The summary line graphs depicted in Fig. 3a illustrate the tumor volumes across various experimental groups of mice, offering a clearer visualization of treatment outcomes. In the control (PBS) group, tumor volumes exhibited a steady increase over time, whereas tumor growth showed some inhibition in groups treated either with sole intraperitoneal injections of αPD-L1 antibody or intratumoral administration of $KMnO_4$. Notably, the combined treatment group exhibited the most pronounced effect, with significantly impeded tumor growth and the lowest increase in volume among all treatment groups. These results underscore the potential synergistic efficacy of co-administering $KMnO_4$ and αPD-L1 antibodies in tumor immunotherapy. The synergistic efficacy of co-administering $KMnO_4$ and αPD-L1 antibodies was also confirmed by the tumor xenograft images retrieved from mice in different treatment groups at the end of the treatment period (Fig. 3b). Significantly, in the group subjected to combined intraperitoneal injections of αPD-L1 antibody and intratumoral administration of $KMnO_4$ (Group IV), an obvious reduction in tumor volume was observed, with two tumors nearly undetectable visually (highlighted with red dashed lines). This strongly suggests a synergistic effect of combined αPD-L1 antibody and $KMnO_4$ intratumoral administration in anti-tumor therapy, significantly inhibiting tumor growth. The *ex vivo* tumor weight statistics of mice across various treatment groups are displayed in Fig. S4 (Supporting information). The quantitative analysis of the average tumor weight in different treatment groups revealed that the control group (Group I) was 1019.66 mg; the group receiving intraperitoneal injections of free αPD-L1 antibody (Group II) was 836.82 mg; the group receiving intratumoral administration of $KMnO_4$ (Group III) was 732.26 mg; and the combined treatment group (Group IV) was only 76 mg. Comparative analysis showed that the tumor inhibition rate in the group receiving intraperitoneal injections of free αPD-L1 antibody was approximately 17.93%, which increased to 28.19% in the $KMnO_4$ intratumoral administration group, while the combined treatment group exhibited the most significant inhibition rate, reaching an astonishing 92.55%. These results collectively indicate that tumor growth is significantly inhibited under the treatment strategy involving the combination of αPD-L1 antibody and $KMnO_4$, thus clearly illustrating the potential of the combined therapy with $KMnO_4$ and αPD-L1 antibody in controlling and reducing tumor growth.

Furthermore, to comprehensively assess the efficacy of different treatment modalities on tumor-bearing mice, we defined tumor growth to 1500 mm^3 as an indicator for euthanasia and ethical termination of mice to obtain a simulated statistical survival curve of mice across the experimental groups, adhering to a humane endpoint criterion. As illustrated in Fig. 3c, the survival curve during the treatment period delineates distinct trends among the experimental cohorts. The PBS control group displayed a precipitous decline in survival rate, with a median survival time of 23 days, indicative of shorter survival in untreated mice. The group receiving intraperitoneal injections of free αPD-L1 antibody (Group II) exhibited a marginally prolonged median survival time of 24 days compared to the control, albeit not as significant as the $KMnO_4$ intratumoral administration group. Notably, the $KMnO_4$ intratumoral administration group (Group III) demonstrated a median survival time of 30 days, suggesting an extension in the survival of mice. Most strikingly, the survival rate in the combined intraperitoneal αPD-L1 antibody and intratumoral $KMnO_4$ treated group (Group IV) declined at the slowest rate among all groups, with a median survival time exceeding 40 days. This outcome vividly underscores the pronounced advantage of $KMnO_4$ combined with immunotherapy in significantly extending mouse survival.

Additionally, during the treatment process, as shown in Fig. S5 (Supporting information), monitoring of the body weight of mice from different experimental groups revealed no abnormal fluctuations throughout the treatment period, with an overall trend of gradual increase over time. This stable growth pattern suggests that under our experimental conditions, none of the treatment regimens had a significant negative impact on the mice, indicating the safety of the various treatment modalities.

In summary, the analysis of volume statistics and observations of *ex vivo* tumor images indicate that the combination therapy involving $KMnO_4$ and αPD-L1 antibody significantly enhances tumor immunotherapy efficacy. This provides robust experimental support for its application in cancer treatment. Particularly noteworthy is the remarkable effectiveness of the combination treatment group, highlighting the potential of this strategy to achieve more effective tumor immunotherapy.

To assess the impact of $KMnO_4$ application on the intratumoral hypoxic microenvironment, the *in vitro* H_2O_2 catalytic activity of the $KMnO_4$-derived BSA-MnO_2 product was confirmed by measuring dissolved O_2 (Fig. S6 in Supporting information), and mice were injected intratumorally with $KMnO_4$ solution, and immunohistochemical staining using hypoxia-inducible factor 1-alpha (HIF-1α) antibody was performed on tumor tissues (Fig. 3d). The distribution of HIF-1α within tumor tissues was visualized in Fig. 3e. The PBS control group exhibited stronger fluorescence signals for HIF-1α, suggesting higher levels of hypoxia in untreated tumor tissues. In contrast, HIF-1α distribution within tumor tissues revealed decreased expression (green signal) in tumors treated with $KMnO_4$, signifying a notable improvement in the intratumoral hypoxic state.

Then, to unravel and deepen the comprehension of the crucial role of $KMnO_4$ in enhancing immune checkpoint blockade therapy

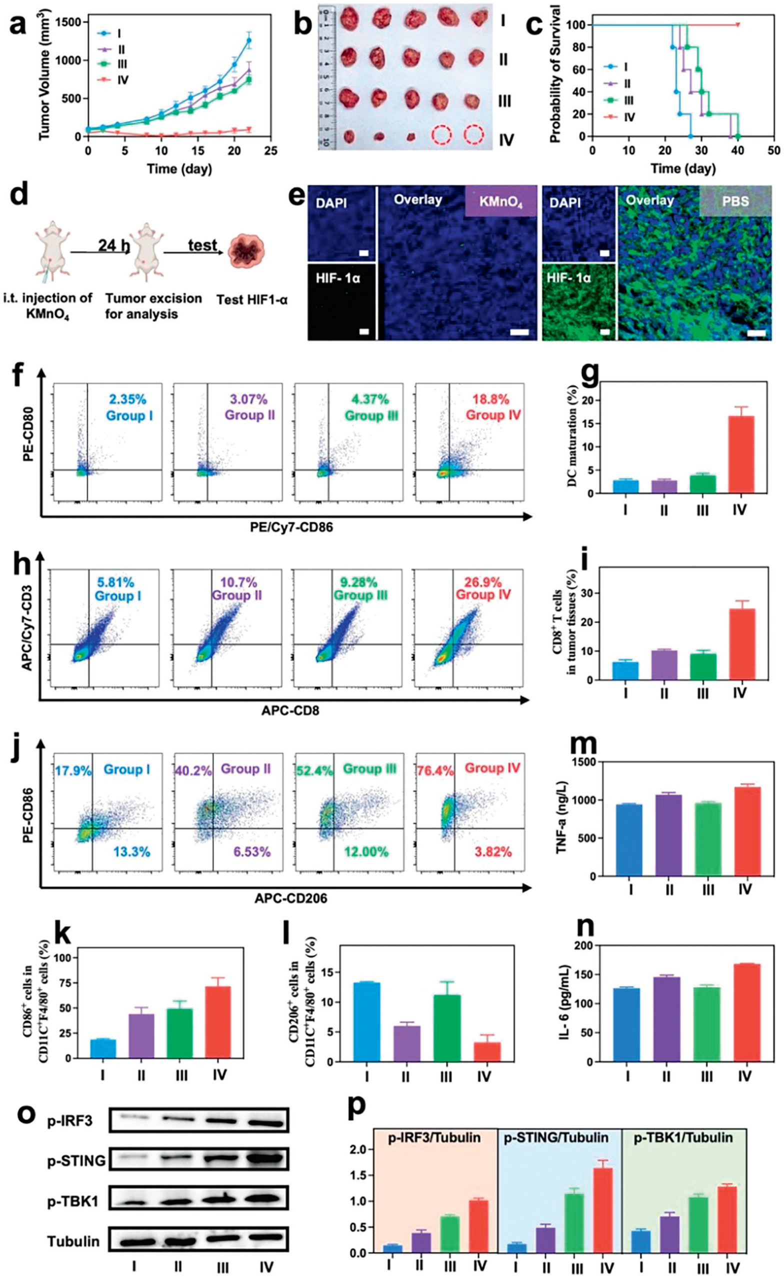

Fig. 3. (a) Consolidated line graph illustrating the tumor volume progression across different experimental mouse groups. (b) *Ex vivo* photographs of tumors harvested from mice at the end of the treatment cycle. (c) Survival curve graph for the different experimental groups of mice. (d) Illustrative diagram of the immunohistochemical assay to assess the mitigation of hypoxic conditions in tumor tissue following intratumoral administration of $KMnO_4$. (e) Fluorescence micrograph of mouse tumor tissue post intratumoral injection with $KMnO_4$, stained with anti-HIF-1α antibody to visualize the localization and expression of HIF-1α. Scale bar: 100 µm. (f, g) Flow cytometric analysis of DCs within the tumor microenvironment and percentage content of mature DCs in tumor-draining lymph nodes in a 4T1 breast cancer treatment model post-administration of various therapeutic strategies. (h, i) Flow cytometric analysis of intratumoral $CD8^+$ T cells (a) and their percentage content (b) following treatment in a 4T1 breast cancer model. (j) Flow cytometric analysis of TAMs within the tumor milieu post-treatment in the 4T1 breast cancer model and proportion of M1-type (k) and M2-type (l) macrophages in the tumor microenvironment. (m, n) Quantification of immune cytokines TNF-α and IL-6 within the tumor tissue was determined using the enzyme-linked immunosorbent assay (ELISA) kits post-therapy. (o, p) Western blot analysis revealing the expression and secretion of key proteins IRF3, STING, and TBK1 within the tumor tissues under different treatment regimens in a breast cancer model. The experimental groups are as follows: (I) PBS (control group); (II) intraperitoneal injection of free αPD-L1 antibody; (III) intratumoral $KMnO_4$ administration; (IV) combined intraperitoneal αPD-L1 antibody and intratumoral $KMnO_4$ treatment. Data are presented as mean ± SD ($n = 3$).

(ICB), the impact of intratumoral $KMnO_4$ administration on the tumor hypoxic microenvironment was investigated *in vivo*. Additionally, the quantities of $CD8^+$ T cells, macrophages, and the proportion of mature DCs within tumor tissues among different treatment groups were analyzed and compared. Furthermore, to analyze the significant impact of $KMnO_4$ application on cGAS-STING activation in mice during tumor treatment, Western blot experiments were conducted on tumor tissues from various experimental groups.

For a more profound understanding of $KMnO_4$'s crucial role in augmenting ICB, this study further conducted meticulous immunocyte analyses on organs and tissues from mice in different experimental groups following treatment. Through flow cytometry, DCs extracted from tumor-draining lymph nodes were assessed for the expression of $CD80^+$ and $CD86^+$ to evaluate DC maturation. As illustrated in Figs. 3f and g, the average expression level of CD86 on the surface of DCs in the combination treatment group was 16.63%. This demonstrated a significant enhancement of at least 4.5 times compared to the sole αPD-L1 antibody treatment group (average 2.74%) and the intratumoral $KMnO_4$ treatment group (average 3.83%), highlighting the pronounced advantage of combination therapy in promoting DC maturation.

Furthermore, quantitative analysis was conducted on the infiltration level of $CD8^+$ T cells and the number of macrophages within tumor tissues. Preliminary findings suggest that the increase in the proportion of $CD8^+$ T cells was more pronounced in the combined treatment group, with an average of 24.63%, compared to 10.24% in the sole αPD-L1 antibody group and 9.09% in the $KMnO_4$ intratumoral administration group (Figs. 3h and i). The combined treatment group exhibited an increase of nearly 2.4-fold, highlighting the significant efficacy of the combined therapy in activating immune responses. These results indicate that $KMnO_4$ may not only directly improve the tumor microenvironment but also potentially exert anti-tumor effects by enhancing T cell-mediated immune responses.

Moreover, concerning the alterations in TAMs, the proportion of M1-type macrophages in the combined treatment group (average 71.4%) far exceeded that in the sole αPD-L1 antibody group (average 44%) and the $KMnO_4$ intratumoral administration group (average 49.23%), while the average proportion of M2-type macrophages in the combined treatment group decreased to 3.26%, significantly lower than the other two single treatment groups (Figs. 3g–l). This underscores the unique role of combined therapy in inducing a shift in the tumor immune microenvironment towards a pro-inflammatory phenotype.

Meanwhile, in the comparison of cytokine secretion levels, the average content of the tumor necrosis factor alpha (TNF-α) in the combined treatment group was 1169.01 pg/mL (Fig. 3m), significantly higher than that in the sole αPD-L1 antibody group (1068.24 pg/mL) and the $KMnO_4$ intratumoral administration group (959.36 pg/mL). For interleukin 6 (IL-6), the average content in the combined treatment group was 168.27 pg/mL, also higher than in the single treatment groups (Fig. 3n). Finally, in the semi-quantitative analysis of Western blot bands, the phosphorylation levels of the interferon regulatory factor 3 (IRF3), STING, and TANK-binding kinase 1 (TBK1) were significantly higher in the combined treatment group compared to either the sole αPD-L1 antibody or the KMnO intratumoral administration group, indicating a pronounced activation of the cGAS-STING pathway under the combined treatment condition (Figs. 3o and p).

Also, blood routine and biochemical parameters were evaluated in mice at the end of each treatment cycle to assess the biological safety of the aforementioned various treatment strategies *in vivo* (Fig. S7 in Supporting information). The data presented include liver function indicators such as aspartate aminotransferase (AST) and alkaline phosphatase (ALP), kidney function indicators such as urea and creatinine (CREA), as well as blood routine indicators including red blood cells (RBC), white blood cells (WBC), hemoglobin (HGB), and platelets (PLT). All parameters in each group fall within the normal range, indicating that the different treatment methods employed in the experiment have good biological safety and did not cause significant organ dysfunction (Figs. S7a–h in Supporting information). Additionally, tissue histopathological evaluation of major organs in mice was conducted using hematoxylin and eosin (H&E) staining at the end of each treatment cycle. This experiment aimed to assess the biological safety of different treatment regimens from a tissue structural perspective. The experimental groups were the same as mentioned above, including the heart, liver, spleen, lungs, and kidneys, among other major organs. As seen in the images, the organ tissue structures remained intact in all treatment groups, with no evident pathological changes, further confirming the safety of the various treatment methods. These results indicate that neither the sole use of αPD-L1 antibody, $KMnO_4$, nor their combined therapy adversely affected the vital organs of mice, providing crucial safety data support for the subsequent clinical application of treatment regimens.

In this study, we systematically explored the bioactivity of $KMnO_4$ and its potential to augment cancer immunotherapy. A series of *in vitro* models indicates that $KMnO_4$ can promote the *in situ* generation of MnO_2 within tumor cells, biomolecules, and solid-state biological tissues, which further undergo reductive conversion to Mn^{2+} in reductive tumor-simulated microenvironments. This interaction provides a basis for biomedical applications of $KMnO_4$ in enhancing tumor immunotherapies. The *in vitro* data suggest that the stimulation of 4T1 cells by $KMnO_4$ induces oxidation damage and immunogenic changes. In combination with αPD-L1 antibodies, $KMnO_4$ significantly inhibited tumor growth, increased survival in tumor-bearing mice, and improved immune response *via* the activation of the cGAS-STING pathway without significant adverse effects. This research supports $KMnO_4$ as a promising anticancer agent and immunotherapy adjuvant, suggesting further investigation into its clinical applicability and long-term effectiveness.

Declaration of competing interest

The authors declare that they have no known competing financial interests or personal relationships that could have appeared to influence the work reported in this paper.

CRediT authorship contribution statement

Kun Chen: Writing – original draft, Software, Methodology, Investigation, Formal analysis, Data curation, Conceptualization. **Huimin Lin:** Writing – original draft, Resources, Methodology, Investigation, Conceptualization. **Xin Peng:** Writing – original draft, Methodology, Formal analysis, Data curation, Conceptualization. **Ziying Wu:** Writing – original draft, Methodology, Investigation, Data curation. **Jingyue Dai:** Resources, Methodology, Conceptualization. **Yi Sun:** Methodology, Investigation. **Yaxuan Feng:** Investigation. **Ziyi Huang:** Investigation. **Zhiqiang Yu:** Writing – review & editing, Supervision, Resources, Conceptualization. **Meng Yu:** Writing – review & editing, Visualization, Supervision, Funding acquisition, Conceptualization. **Guangyu Yao:** Writing – review & editing, Supervision, Project administration, Funding acquisition, Conceptualization. **Jigang Wang:** Writing – review & editing, Validation, Supervision, Resources, Project administration, Funding acquisition, Conceptualization.

Acknowledgments

This work was supported by the Natural Science Foundation of Guangdong Province (No. 2023A1515030291), the Dongguan Science and Technology of Social Development Program (No. 20211800905282); the National Key Research and Development Program of China (Nos. 2022YFC2303600, 2020YFA0908000); the Innovation Team and Talents Cultivation Program of National Administration of Traditional Chinese Medicine (No. ZYYCXTD-C-202002); the CACMS Innovation Fund (Nos. CI2023E002, CI2021A05101, CI2021A05104); the Scientific and Technological Innovation Project of China Academy of Chinese Medical Sciences (Nos. CI2023D003, CI2021B014); the Science and Technology Foundation of Shenzhen (No. JCYJ20210324115800001), the Science and Technology Foundation of Shenzhen (Shenzhen Clinical Medical Research Center for Geriatric Diseases); the Shenzhen Medical Research Fund (No. B2302051); the Distinguished Expert Project of

Sichuan Province Tianfu Scholar (No. CW202002); Shenzhen Science and Technology Program (No. RCBS20210609104424065).

Supplementary materials

Supplementary material associated with this article can be found, in the online version, at doi:10.1016/j.cclet.2024.110045.

References

[1] B. Wang, J. Zhou, R. Li, et al., Adv. Mater. 36 (2024) 2311640.
[2] Q. Li, M. Dang, J. Tao, et al., Adv. Funct. Mater. 34 (2024) 2311480.
[3] W. Zeng, Z. Li, Q. Huang, et al., Adv. Funct. Mater. 34 (2023) 2307241.
[4] D.R. Wang, X.L. Wu, Y.L. Sun, Signal Transduct. Target. Ther. 7 (2022) 331.
[5] X. Wang, Y. Liu, C. Xue, et al., Nat. Commun. 13 (2022) 5685.
[6] P. Sun, Z. Li, D. Zhang, et al., Chin. Chem. Lett. 35 (2024) 108346.
[7] X. Li, C. Shao, Y. Shi, W. Han, J. Hematol. Oncol. 11 (2018) 31.
[8] Y. Mi, C.T. Hagan 4th, B.G. Vincent, A.Z. Wang, Adv. Sci. 6 (2019) 1801847.
[9] W. Ma, R. Sun, L. Tang, et al., Adv. Mater. 35 (2023) 2303149.
[10] B. Zhang, Y. Wang, S. Wang, et al., Adv. Funct. Mater. 33 (2023) 2305630.
[11] Q. Li, Z. Teng, J. Tao, et al., Small 18 (2022) 2201108.
[12] L. Zhang, L. Xu, Y. Wang, et al., Chin. Chem. Lett. 33 (2022) 4089–4095.
[13] Z. Feng, G. Chen, M. Zhong, et al., Biomaterials 302 (2023) 122333.
[14] D. Wei, J. Fan, J. Yan, et al., J. Am. Chem. Soc. 146 (2024) 1185–1195.
[15] X. Sun, Y. Wang, T. Du, et al., Chin. Chem. Lett. 34 (2023) 108201.
[16] J. Wan, X. Zhang, D. Tang, T. Liu, H. Xiao, Adv. Mater. 35 (2023) e2209799.
[17] B. Zhang, L. Lin, J. Mao, et al., Chin. Chem. Lett. 34 (2023) 108518.
[18] J. Wang, Q. Zhang, Y. Li, et al., Chin. Chem. Lett. 35 (2024) 108746.
[19] H. Zhu, K. Ma, R. Ruan, et al., Chin. Chem. Lett. 35 (2024) 108536.
[20] J. Gao, H. Zhang, F. Zhou, et al., Chin. Chem. Lett. 32 (2021) 1929–1936.
[21] K. Zhang, C. Qi, K. Cai, Adv. Mater. 35 (2023) e2205409.
[22] N. Jiang, Z. Zhou, W. Xiong, et al., Chin. Chem. Lett. 32 (2021) 3948–3953.
[23] X. Sun, Y. Zhang, J. Li, et al., Nat. Nanotechnol. 16 (2021) 1260–1270.
[24] M. Lv, M. Chen, R. Zhang, et al., Cell Res. 30 (2020) 966–979.
[25] B. Ding, P. Zheng, P. Ma, J. Lin, Adv. Mater. 32 (2020) e1905823.
[26] L. Hou, C. Tian, Y. Yan, et al., ACS Nano 14 (2020) 3927–3940.
[27] W. Zhang, S. Li, X. Liu, et al., Adv. Funct. Mater. 28 (2018) 1706375.
[28] S. Huang, Y. Gao, H. Li, et al., Adv. Mater. 36 (2024) e2310979.
[29] T. He, X. Qin, C. Jiang, et al., Theranostics 10 (2020) 2453–2462.
[30] J. Azadmanesh, G.E.O. Borgstahl, Antioxidants 7 (2018) 25.
[31] G. Sokhi, Br. J. Cancer 24 (1970) 290–293.
[32] J. Tao, Y. Tian, D. Chen, et al., Angew. Chem. Int. Ed. 62 (2023) e202216361.
[33] M.C. Biesinger, B.P. Payne, A.P. Grosvenor, et al., Appl. Surf. Sci. 257 (2011) 2717–2730.